



HAL
open science

Last Glacial Maximum temperature in the Alps quantified using luminescence paleothermometry

Rabiul Biswas, Vjeran Višnjević, Florence Magnin, Benjamin Lehmann,
Georgina King, Frédéric Herman

► **To cite this version:**

Rabiul Biswas, Vjeran Višnjević, Florence Magnin, Benjamin Lehmann, Georgina King, et al.. Last Glacial Maximum temperature in the Alps quantified using luminescence paleothermometry. 2020. hal-03024184

HAL Id: hal-03024184

<https://hal.science/hal-03024184v1>

Preprint submitted on 25 Nov 2020

HAL is a multi-disciplinary open access archive for the deposit and dissemination of scientific research documents, whether they are published or not. The documents may come from teaching and research institutions in France or abroad, or from public or private research centers.

L'archive ouverte pluridisciplinaire **HAL**, est destinée au dépôt et à la diffusion de documents scientifiques de niveau recherche, publiés ou non, émanant des établissements d'enseignement et de recherche français ou étrangers, des laboratoires publics ou privés.

1 **Last Glacial Maximum temperature in the Alps quantified using**
2 **luminescence paleothermometry**

3 **Rabiul Biswas¹, Vjeran Višnjević¹, Florence Magnin², Benjamin Lehmann¹,**
4 **Georgina King¹, Frédéric Herman¹**

5 Corresponding author: frederic.herman@unil.ch

6 ¹: Institute of Earth Surface dynamics, University of Lausanne, Switzerland

7 ²: Laboratoire EDYTEM, Université Savoie Mont-Blanc, France

8 **The Last Glacial Maximum (LGM) corresponds to the most recent time when ice-**
9 **sheets and ice-caps globally reached their maximum integrated volume.**
10 **Quantifying how cold it was remains challenging, especially in regions that were**
11 **entirely covered by ice. Climate records are often not well preserved, thereby**
12 **restricting the use of existing climate proxies. Here we demonstrate that the mean**
13 **annual temperature in the western Alps was 8.8 ± 2.1 °C cooler at the end of the**
14 **LGM than present by measuring the temperature history recorded in rocks using**
15 **thermoluminescence of feldspar. These results are consistent with climatic**
16 **reconstructions inferred from the detailed geomorphic mapping of the ice-cap that**
17 **covered the Alps. Our results imply that climate was considerably colder than the**
18 **global average and substantially drier in central western Europe compared to**
19 **present.**

20 The Last Glacial Maximum (LGM) lasted from about 33 kyr to about 17 kyr ago
21 and corresponds to the largest and probably best-documented climate change in recent
22 Earth history (1). Climate was generally drier and temperatures were globally lower.
23 Cooling led to the expansion of polar ice-sheets and icecaps at high latitudes and on
24 sufficiently high mountain ranges, but what the actual temperature was during the LGM
25 remains uncertain. Despite a long history of research (2), estimates of mean global
26 temperature vary widely from 1.7 to 8 °C lower than present (3-9). In addition, such
27 global temperatures mask even larger regional temperature fluctuations. Quantifying
28 regional variations is particularly important to understand climate dynamics as regional
29 temperature differences cause pressure gradients that govern the distribution of heat
30 and moisture on Earth.

1 In that context, the LGM European continental climate is particularly elusive.
2 Temperature and precipitation in western Europe are primarily controlled by the
3 position and intensity of the jet stream and storm track. The decrease of greenhouse gas
4 concentrations in the atmosphere and the presence of large ice sheets during the LGM
5 caused a decrease in temperature that increases with increasing latitude. Such a
6 strengthening of the equator to pole temperature gradient likely affected the position and
7 intensity of the jet stream and storm track, and thus European climate. This problem has
8 been the focus of numerous modeling studies (10-14), which often argue for a more
9 zonally oriented atmospheric jet stream during the LGM compared to present (12,15) but
10 predict surprisingly different temperature and precipitation patterns over western
11 Europe (11,13,14). These differences are even further exacerbated by their longstanding
12 disagreement (10,14) with climate reconstructions based on pollen (16-18) or stable
13 isotope in groundwater (19) and speleothems (20).

14 The western Alps host the highest topography in central western Europe and form
15 an important physical boundary that strongly influences the climate of surrounding
16 regions. During the LGM, the Alps were entirely covered by a large ice-cap that reflected
17 climatic conditions in Europe at that time (21-23). The ice extent reflects temperature,
18 precipitation and insolation, but the ensemble of temperature and precipitation
19 combinations that can explain the observed ice extent is non-unique and varies spatially
20 (22). Furthermore, there still exist large uncertainties concerning the ice thickness (23)
21 although the ice extent is well documented (24). As a result, it is not possible to
22 discriminate precipitation and temperature changes using the ice extent alone. One must
23 acquire independent estimates of temperature or precipitation to constrain the climatic
24 conditions that prevailed in central Europe during the LGM.

25 To independently constrain how temperature changed between the LGM and the
26 present, we collected samples along a 500 m vertical profile on the valley flanks of the
27 Mer de Glace, one of the largest glaciers in the Alps which retreated since about 19-17 kyr
28 ago (25-26). We collected samples on steep slopes, which only accumulate limited
29 amounts of snow in winter (Fig. 1). The rocks have been exposed to atmospheric
30 conditions since the end of LGM and thus provide a record of atmospheric temperature
31 since that time. We reconstructed the temperature history of each rock using a new
32 method based on thermoluminescence of feldspar (27). The principle of the approach
33 consists of translating the abundance of trapped electrons in the crystalline lattice into

1 corresponding time-temperature histories (27; Supplementary Materials). Using a well-
2 calibrated physical model combined with a Bayesian approach, we reconstruct the mean
3 annual temperature since the end of the LGM. In comparison to other existing proxies,
4 our method does not rely on numerous climatic assumptions such as seasonality,
5 precipitation, plant-available moisture, the length of the growing season (16-18) or the
6 preservation of organic compounds (28).

7 Our results show that the temperature difference between the LGM and the
8 present is about 9 °C for all samples (Fig. 2). The thermoluminescence method yields rock
9 temperatures that are higher than atmospheric mean annual temperatures. However, it
10 is expected that the temperature in rocks exhibit an offset with atmospheric temperature
11 depending on their exposure to solar radiation, their color and the amount of snow cover
12 (29). We compare our results to temperatures estimated from a statistical relationship
13 between air temperature and measured rock temperature used to characterize rock
14 permafrost (29). The results show a good match between the two approaches (Fig. 2).
15 Combining all the luminescence measurements, we find a temperature difference
16 between the LGM and the present of 8.8 ± 2.1 °C. The constant temperature difference
17 with altitude also indicates that the lapse rate did not change between the LGM and today,
18 and remained about 0.55 °C per 100 m.

19 Višnjević et al. (22) recently inverted the ice extent for the entire Alps into spatially
20 variable equilibrium line altitudes (ELAs) (Supplementary Materials). The ELA is the
21 most useful parameter to quantify the effect of climate on glaciers and icecaps. It defines
22 the altitude where the annual accumulation of snow is equal to the ablation, and it
23 primarily depends on winter precipitation and mean annual temperature. They ran 25
24 inversions (22) that we complement with 12 additional inversions to find the ELA maps
25 (Fig. 3) that best explain the observed ice extent. Then we translate the LGM ELA maps
26 into mean annual temperatures and winter accumulation rates at the Mer de Glace, using
27 the prescribed accumulation rate and our observation that the altitudinal temperature
28 lapse rate did not change between the end of the LGM and the present (Supplementary
29 Materials). The temperature histories inferred from thermoluminescence are local but
30 the inversion of the ice extent enables us to integrate information at the scale of the Alps.
31 Furthermore, our calculations illustrate the tradeoff that exists between temperature and
32 precipitation when using the past ice extent as sole information (22-23).

1 The combination of our results imply that climate in the Alps was colder at the end
2 of the LGM by about 9°C and more likely between 50 and 85% drier than it currently is
3 (Fig. 4). The estimated temperature difference also matches the results from an
4 independent ice-extent reconstruction that assumes that precipitation patterns at the
5 LGM were identical to present but that climate was about 50% drier (23). More
6 importantly, temperatures in the Alps at the end of the LGM were cooler than the recently
7 estimated -6.1 °C global cooling (9). Estimates of global averages are overwhelmingly
8 based on marine sea surface temperature records and models. Our results imply that
9 temperature differences between the end of the LGM and the present can be larger in
10 regions that were entirely covered by ice. If these locations were included, estimated
11 global average temperature would be lower.

12 Inferences of past climate in the Alps have so far relied on the analysis of fossil
13 assemblages of biota and pollen preserved in lake sediments and peat (30), the analysis
14 of oxygen isotopes in speleothems (e.g., 20), lake sediments (e.g., 31) and groundwater
15 (19), or the analysis of past soil formation processes (30). Although the existing records
16 show that climate in the Alps likely followed the Greenland oxygen isotope record (30),
17 there is currently no climate record that span the last 20 kyr continuously. The ice-cap
18 that covered the Alps prevented vegetation to grow and thereby produce the necessary
19 climate archive. Additionally, uncertainties on the atmospheric conditions during the
20 LGM have made the conversion of most climate proxies into LGM temperature and
21 precipitation particularly challenging (30). The fossil pollen records suggest that the
22 mean annual temperature difference between the LGM and today is somewhere between
23 10 and 15 °C (16,18). Our results provide us with slightly lower temperature estimates.
24 Interestingly, lower temperature differences are in better agreement with existing
25 climate simulations (10,14).

26 Our findings that temperatures at the end of the LGM were 8.8 ± 2.1 °C lower than
27 present and possibly up to 85% drier suggest that an increase of moisture related to a
28 large southward shift of the storm track trajectories that would lead to an increase of
29 atmospheric moisture in the Alps is rather unlikely (20,21). Instead, our results are more
30 consistent with a range of atmospheric models (14) and in particular those suggesting a
31 more zonally oriented atmospheric jet stream and storm track during the LGM (12,15).
32 These models predict a southward shift of the jet stream that only extended south of the
33 Scandinavian ice cap (12) and primarily happened in summer (11) during the LGM.

1 References

- 2 1. Clark, P.U., Dyke, A.S., Shakun, J.D., Carlson, A.E., Clark, J., Wohlfarth, B., Mitrovica,
3 J.X., Hostetler, S.W., McCabe, A.M. The last glacial maximum. *Science*, **325(5941)**,
4 710-714 (2009).
- 5 2. CLIMAP Project Members. The surface of the ice-age earth. *Science*, **191(4232)**,
6 1131-1137 (1976).
- 7 3. Schneider von Deimling, T., Ganopolski, A., Held, H. & Rahmstorf, S. How cold was
8 the last glacial maximum? *Geophysical Research Letters*, **33(14)** (2006).
- 9 4. Holden, P.B., Edwards, N.R., Oliver, K.I.C., Lenton, T.M., Wilkinson, R.D.. A
10 probabilistic calibration of climate sensitivity and terrestrial carbon change in
11 GENIE-1. *Climate Dynamics*, **35(5)**, 785-806 (2010).
- 12 5. Schmittner, A., Urban, N.M., Shakun, J.D., Mahowald, N.M., Clark, P.U., Bartlein, P.J.,
13 Mix, A.C., Rosell-Melé, A. Climate sensitivity estimated from temperature
14 reconstructions of the Last Glacial Maximum. *Science*, **334(6061)**, 1385-1388
15 (2011).
- 16 6. Shakun, J.D., Clark, P.U., He, F., Marcott, S.A., Mix, A.C., Liu, Z., Otto-Bliesner, B.,
17 Schmittner, A., Bard, E.. Global warming preceded by increasing carbon dioxide
18 concentrations during the last deglaciation. *Nature*, **484(7392)**, 49-54 (2012).
- 19 7. Annan, J.D. and Hargreaves, J.C.. A new global reconstruction of temperature
20 changes at the Last Glacial Maximum. *Climate of the Past*, **9(1)**, 367-376 (2013).
- 21 8. Bereiter, B., Shackleton, S., Baggenstos, D., Kawamura, K., Severinghaus, J. Mean
22 global ocean temperatures during the last glacial transition. *Nature*, **553(7686)**,
23 39-44 (2018).
- 24 9. Tierney, J. E., Zhu, J., King, J., Malevich, S. B., Hakim, G., & Poulsen, C. Glacial
25 cooling and climate sensitivity revisited. *Nature*, (in press)
- 26 10. Kageyama, M., Lâiné, A., Abe-Ouchi, A., Braconnot, P., Cortijo, E., Crucifix, M., De
27 Vernal, A., Guiot, J., Hewitt, C.D., Kitoh, A., Kucera, M. Last Glacial Maximum
28 temperatures over the North Atlantic, Europe and western Siberia: a comparison
29 between PMIP models, MARGO sea-surface temperatures and pollen-based
30 reconstructions. *Quaternary Science Reviews*, **25(17-18)**, 2082-2102 (2006).
- 31 11. Beghin, P., Charbit, S., Kageyama, M., Combourieu-Nebout, N., Hatté, C., Dumas, C.,
32 Peterschmitt, J.Y. What drives LGM precipitation over the western
33 Mediterranean? A study focused on the Iberian Peninsula and northern
34 Morocco. *Climate Dynamics*, **46(7-8)**, 2611-2631 (2016).
- 35 12. Löffverström, M., Caballero, R., Nilsson, J., Messori, G. Stationary wave reflection
36 as a mechanism for zonalizing the Atlantic winter jet at the LGM. *Journal of the*
37 *Atmospheric Sciences*, **73(8)**, 3329-3342 (2016).
- 38 13. Ludwig, P., Schaffernicht, E.J., Shao, Y., Pinto, J.G. Regional atmospheric
39 circulation over Europe during the Last Glacial Maximum and its links to
40 precipitation. *Journal of Geophysical Research: Atmospheres*, **121(5)**, 2130-2145
41 (2016).
- 42 14. Kageyama, M., Harrison, S.P., Kapsch, M.L., Löffverström, M., Lora, J.M.,
43 Mikolajewicz, U., Sherriff-Tadano, S., Vadsaria, T., Abe-Ouchi, A., Bouttes, N.,
44 Chandan, D. The PMIP4-CMIP6 Last Glacial Maximum experiments: preliminary
45 results and comparison with the PMIP3-CMIP5 simulations. *Climate of the Past*
46 *Discussions* (2020)

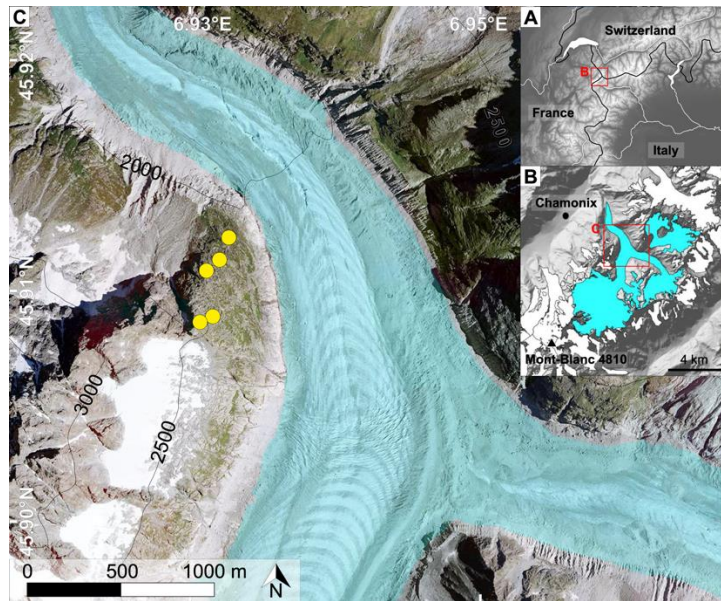
- 1 15. Li, C., Battisti, D.S.. Reduced Atlantic storminess during Last Glacial Maximum:
2 Evidence from a coupled climate model. *Journal of Climate*, 21(14), 3561-3579
3 (2008).
- 4 16. Peyron, O., Guiot, J., Cheddadi, R., Tarasov, P., Reille, M., de Beaulieu, J.L., Bottema,
5 S., Andrieu, V., 1998. Climatic reconstruction in Europe for 18,000 yr BP from
6 pollen data. *Quaternary research*, 49(2), 183-196 (1998).
- 7 17. Bartlein, P.J., Harrison, S.P., Brewer, S., Connor, S., Davis, B.A.S., Gajewski, K.,
8 Guiot, J., Harrison-Prentice, T.I., Henderson, A., Peyron, O., Prentice, I.C. Pollen-
9 based continental climate reconstructions at 6 and 21 ka: a global
10 synthesis. *Climate Dynamics*, 37(3), 775-802 (2011).
- 11 18. Wu, H., Guiot, J., Brewer, S., Guo, Z. Climatic changes in Eurasia and Africa at the
12 last glacial maximum and mid-Holocene: reconstruction from pollen data using
13 inverse vegetation modelling. *Climate Dynamics*, 29(2-3), 211-229 (2007).
- 14 19. Beyerle, U., Purtschert, R., Aeschbach-Hertig, W., Imboden, D.M., Loosli, H.H.,
15 Wieler, R., Kipfer, R. Climate and groundwater recharge during the last glaciation
16 in an ice-covered region. *Science*, 282(5389), 731-734 (1998).
- 17 20. Luetscher, M., Boch, R., Sodemann, H., Spötl, C., Cheng, H., Edwards, R.L., Frisia, S.,
18 Hof, F., Müller, W. North Atlantic storm track changes during the Last Glacial
19 Maximum recorded by Alpine speleothems. *Nature Communications*, 6(1), 1-6
20 (2015).
- 21 21. Florineth, D., Schlüchter, C. Reconstructing the Last Glacial Maximum (LGM) ice
22 surface geometry and flowlines in the Central Swiss Alps. *Eclogae Geologicae*
23 *Helveticae*, 91, 91-407 (1998).
- 24 22. Višnjević, V., Herman, F., Prasicek, G. Climatic patterns over the European Alps
25 during the LGM derived from inversion of the paleo-ice extent. *Earth and*
26 *Planetary Science Letters*, 538, 116-185 (2020).
- 27 23. Seguinot, J., Ivy-Ochs, S., Jouvet, G., Huss, M., Funk, M., Preusser, F. Modelling last
28 glacial cycle ice dynamics in the Alps. *The Cryosphere*, 12(10), 3265-3285
29 (2018).
- 30 24. Ehlers, J., Gibbard, P.L., Hughes, P.D. *Quaternary glaciations-extent and*
31 *chronology: a closer look* (Vol. 15). Elsevier. (2011)
- 32 25. Wirsig, C., Zasadni, J., Christl, M., Akçar, N., Ivy-Ochs, S. Dating the onset of LGM
33 ice surface lowering in the High Alps. *Quaternary Science Reviews*, 143, 37-50
34 (2016).
- 35 26. Lehmann, B., Herman, F., Valla, P.G., King, G.E., Biswas, R.H., Ivy-Ochs, S.,
36 Steinemann, O., Christl, M.. Postglacial erosion of bedrock surfaces and
37 deglaciation timing: New insights from the Mont Blanc massif (western
38 Alps). *Geology*, 48(2), 139-144 (2020).
- 39 27. Biswas, R.H., Herman, F., King, G.E., Lehmann, B., Singhvi, A.K. Surface
40 paleothermometry using low temperature thermoluminescence of
41 feldspar. *Climate of the Past Discussions*, 1-26 (2020).
- 42 28. Schouten, S., Hopmans, E.C., Damsté, J.S.S.. The organic geochemistry of glycerol
43 dialkyl glycerol tetraether lipids: a review. *Organic geochemistry*, 54, 19-61
44 (2013).
- 45 29. Magnin, F., Deline, P., Ravanel, L., Noetzli, J., Pogliotti, P. Thermal characteristics
46 of permafrost in the steep alpine rock walls of the Aiguille du Midi (Mont Blanc
47 Massif, 3842 m asl). *The Cryosphere*, 9(1), 109-121 (2015).
- 48 30. Heiri, O., Koinig, K.A., Spötl, C., Barrett, S., Brauer, A., Drescher-Schneider, R.,
49 Gaar, D., Ivy-Ochs, S., Kerschner, H., Luetscher, M., Moran, A. Palaeoclimate

1 records 60–8 ka in the Austrian and Swiss Alps and their forelands. *Quaternary*
2 *Science Reviews*, **106**, 186-205 (2014).
3 31. Lauterbach, S., Brauer, A., Andersen, N., Danielopol, D.L., Dulski, P., Hüls, M.,
4 Milecka, K., Namiotko, T., Obremaska, M., Von Grafenstein, U., Declakes
5 Participants. Environmental responses to Lateglacial climatic fluctuations
6 recorded in the sediments of pre-Alpine Lake Mondsee (northeastern
7 Alps). *Journal of Quaternary Science*, **26(3)**, 253-267 (2011).
8

9 **Acknowledgements**

10 The authors Basil Davis for discussions and feedback on the manuscript. The
11 luminescence data and codes are available on
12 https://github.com/ciredorf13/TL_paleothermometry. The data and code for the
13 inversion of past ice extents into ELA are available **on XXX**. Temperature data used to
14 estimate rock temperature are available **on XXX**.

1 Figures

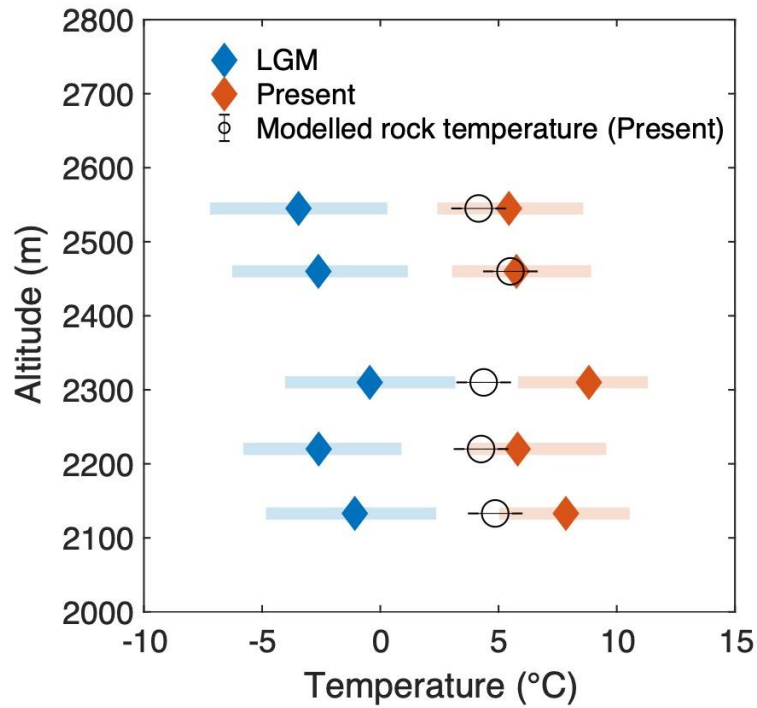


2

3 **Figure 1: Samples location.** (A) Digital elevation model of the Alps. (B) Mont Blanc
4 Massif. (C) Mer de Glace. The yellow dots show the location of the analyzed samples. The
5 red boxes in (A) and (B) show the location of (B) and (C).

6

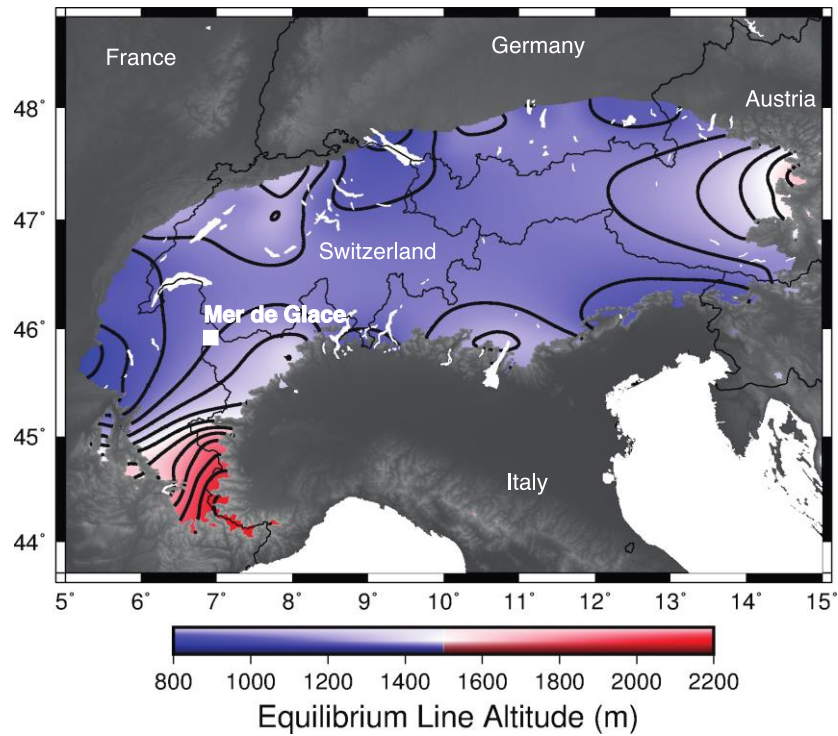
1



2

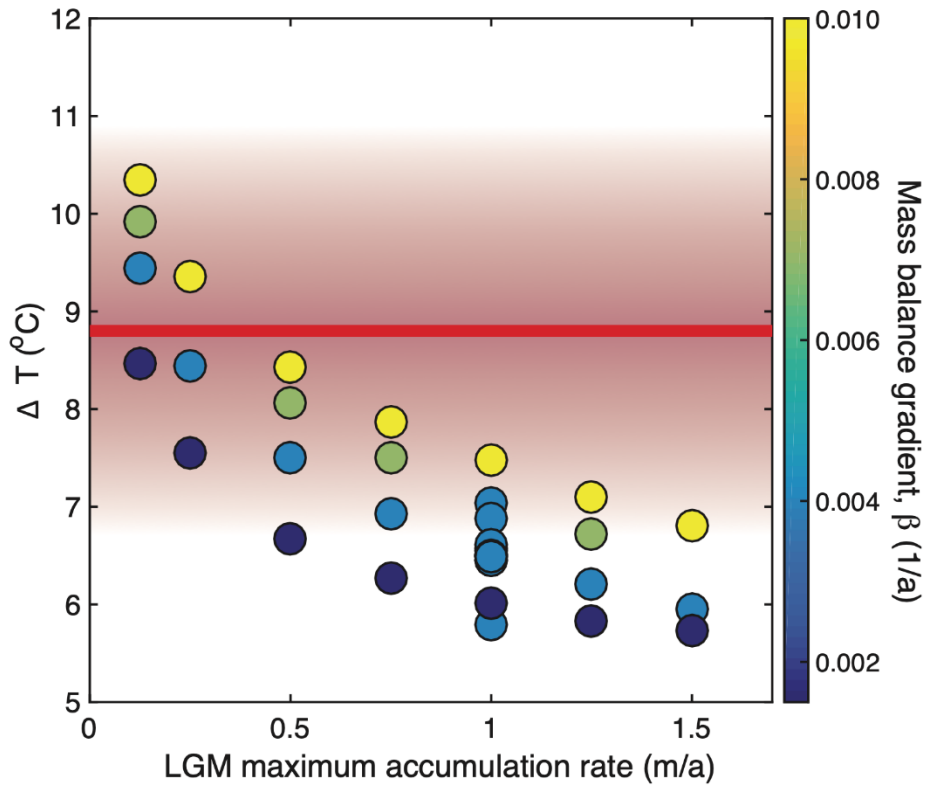
3 **Figure 2: Temperature difference between LGM temperature and present-day**
4 **temperature.** The blue and red diamonds depict temperature at the end of the LGM and
5 present-day respectively inferred using thermoluminescence, and the black circles depict
6 present-day temperatures estimated from a statistical relationship between air
7 temperature and measured rock temperature (Supplementary Materials).

8



1
 2 **Figure 3: LGM Equilibrium Line Altitude (ELA) inferred from the inversion of the**
 3 **observed LGM ice extent (24).** The white square shows the location of the Mer de Glace.
 4 The thin black lines depict the political borders. The thick black line are 100 m contour
 5 lines of ELA. For this inversion β is equal to 0.01 1/a and c to 0.25 m/a, which corresponds
 6 to a temperature difference between the LGM and the present at the Mer de Glace equal
 7 to 8.5 °C.

1
2



3
4
5
6
7
8
9
10
11

Figure 4: LGM accumulation rates and temperature difference at the Mer glacier inferred from the inversion the LGM ice extent into ELAs. The dots depict the temperature difference between the end of the LGM and the present inferred for individual inversion of ice extent into an ELA field (Supplementary Materials). The color associated with each dot represents the mass balance gradient used for each individual inversion. The red line is the temperature difference inferred using thermoluminescence and its error.



Supplementary Materials for

Last Glacial Maximum temperature in the Alps quantified using luminescence paleothermometry

Rabiul Biswas¹, Vjeran Višnjević¹, Florence Magnin², Benjamin Lehmann¹, Georgina King¹, Frédéric Herman¹

Corresponding author: frederic.herman@unil.ch

¹: Institute of Earth Surface dynamics, University of Lausanne, Switzerland

²: Laboratoire EDYTEM, Université Savoie Mont-Blanc, France

This PDF file includes:

Materials and Methods
Figs. S1 to S5
Tables S1

1. Materials

Samples: Five bedrock samples were collected at the Mer de Glace glacier (Mont Blanc massif, European Alps) at altitudes from 2133 to 2545 m. The rocks are phenocrystalline granites of the Mont Blanc massif. All the rocks were collected from glacially eroded bedrock surfaces (26). The sample were located between the ice-surface elevations of the Little Ice Age (LIA) and the LGM (26). All the samples were recently dated using ¹⁰Be terrestrial cosmogenic nuclide and OSL surface exposure dating simultaneously (Lehmann et al., 2020). The top four samples were exposed since the end of the LGM about 17 kyr ago (25-26). Only the bottom sample was exposed between the LGM and the Younger Dryas about 12 kyr ago. The location of the samples is shown in Figure 1.

2. Methods

2.1 Thermoluminescence thermometry

Thermoluminescence of feldspar: Luminescence paleothermochronometry is a recently established technique that is based on the Quaternary dating method of

1 thermoluminescence (TL) dating (32). TL dating relies on the time-dependent
 2 accumulation of electrons in crystal defects that occurs when certain minerals, including
 3 feldspar, are exposed to ionizing radiation from naturally occurring radionuclides (e.g.,
 4 U, Th, and K) as well as cosmic rays. The targeted trapped charge population is thermally
 5 sensitive, which can be exploited to extract thermal histories of rocks. The idea was first
 6 introduced in the sixties for terrestrial applications (33) and seventies for lunar samples
 7 from the Appolo 12 mission (34-35). It was only revived and further developed recently
 8 for terrestrial applications (27). Biswas et al. (27,36) showed that thermoluminescence
 9 signals exhibit a continuum of thermal stability. Each thermal stability range correspond
 10 to a paleothermometer. The combination of several paleothermometer enables the
 11 reconstruction of past temperature histories of rocks with great precision.

12 Theory: TL of feldspar can be described with a rate equation that encapsulates the
 13 process of populating traps with electrons in response to environmental ionizing
 14 radiation and the processes of electron escape through thermal and athermal processes.
 15 We briefly outline the kinetic model here. The reader is referred to Biswas et al. (2020)
 16 (27) for further information.

17 The rate equation for the trapped charge population of a specific trapping center,
 18 with single trap depth (E), frequency factor (s), and athermal fading parameter (ρ' ; 37-
 19 38) is as follows:

$$20 \quad \frac{d}{dt}(\bar{n}(r', t)) = \frac{\dot{D}}{D_0}(1 - \bar{n}(r', t))^a - se^{-\frac{E}{kT}}(\bar{n}(r', t))^b - \tilde{s}e^{-\rho' \frac{1}{3}r'}\bar{n}(r', t) \quad (1)$$

21 where \bar{n} is equal to n/N (where n is the number of trapped electrons at time t and
 22 temperature T , and N is the total number of available traps), \dot{D} is the dose rate due to
 23 ambient radioactivity (Gy kyr^{-1}), D_0 is the characteristic dose (Gy), a and b are the kinetic
 24 orders of trapping and thermal detrapping respectively, E is the trap depth or activation
 25 energy (eV), s and \tilde{s} are the thermal and athermal frequency factor respectively (s^{-1}), ρ' is
 26 the dimensionless athermal fading rate and r' is a dimensionless distance that
 27 characterizes the probability of athermal escape (38). A key element is that a , b , \dot{D} , D_0 , E ,
 28 s and ρ' are constrained from laboratory experiments for each sample (Biswas et al.,
 29 2018; 2020).

1 To account for athermal loss, i.e., anomalous fading (39), the total number of
2 trapped electrons at any instant $\bar{n}(t)$ is obtained by integrating over the whole range of
3 dimensionless distances ($0 < r' < 2; 40$) over which electrons can athermally escape;

$$4 \quad \bar{n}(t) = \int_0^{\infty} p(r') \bar{n}(r', t) dr' \quad (2)$$

5 where $p(r')$ is the probability of nearest recombination center at a distance between r'
6 and $r'+dr'$ and expressed as $p(r')dr' = 3r'^2 e^{-r'^3} dr'$ (38).

7 This model was validated using rocks from the KTB borehole and applied to
8 samples from Namche Barwa (36), which gave results in agreement with other studies
9 from the same area (41).

10 It has been established that TL of feldspar arises from a continuous distribution of
11 trap energies (36, 42-45) and that the TL processes is reflected by the sum of a large
12 number of traps (36, 44); all follow the process described by Equation 1. The kinetic
13 parameters are constrained from laboratory-controlled experiments (27,36).

14 Sample preparation: The samples were prepared following the method reported in (47).
15 The light exposed outer layer (>2 cm from the surface) was removed using a diamond
16 saw under subdued red-light conditions with constant water flow to avoid frictional
17 heating. The interior part of the sample was gently crushed with a mortar and pestle and
18 sieved to separate the 150–250 μm grain size. The samples were sequentially treated
19 with 10% HCl and 30% H_2O_2 to remove carbonate and organic matter respectively. Once
20 dried, the magnetic fractions were separated and removed using a hand magnet. The K-
21 feldspar fraction was removed by density separation ($<2.58 \text{ gm/cm}^3$) using sodium
22 polytungstate. The grains were mounted on stainless steel discs using Silko-spay. Small
23 aliquots of 2 mm diameter (containing ~ 100 grains) were prepared because the analyzed
24 feldspars were very bright.

25 Luminescence measurements: The TL measurements were made using a Risø TL/OSL
26 reader (48) equipped with a $^{90}\text{Sr}/^{90}\text{Y}$ irradiation source ($\sim 0.24 \text{ Gy/s}$) at the University
27 of Lausanne. A heating rate of $1 \text{ }^\circ\text{C/s}$ was used, under constant flow of N_2 gas. The TL
28 emission was restricted to violet-blue ($395 \pm 30 \text{ nm}$) using a filter combination of BG3 and
29 BG39. A sensitivity correction was applied to the measurements following Biswas et al.
30 (2020). The natural TL or present-day trapped charge population was measured and a
31 sensitivity correction was applied to the measurements following (27).

1 Inversion of TL data into thermal histories: We use a Bayesian approach to invert TL data
2 (\bar{n}_o) into thermal histories. The approach consists of generating a large number of
3 random thermal histories (300,000) and predict \bar{n}_p for each thermal history using
4 Equation 1. We then compare the predicted value to the observed one, \bar{n}_o , and select the
5 thermal histories that provide the best fit to the data. From the selected path, we can then
6 build a probably density function and estimate temperatures at the LGM and the present
7 (27).

8 We assume that the shape of the temperature histories follows the ice core $\delta^{18}\text{O}$
9 Greenland record (48). All the existing records from the Alps follow the Greenland oxygen
10 isotope record (30). However, the records are not continuous during the last 20 kyr, and
11 how temperature varied is unknown and. Here we scale the continuous $\delta^{18}\text{O}$ record from
12 Greenland by varying the minimum temperature (i.e., temperature at ~ 17 kyr ago)
13 between -20 and 20 °C and the maximum amplitude of the temperature change between
14 between 0 and 30 °C (i.e., the difference between minimum the temperature and the
15 maximum temperature).

16 For each thermal history, we assess the quality of fit to the data using the following
17 misfit function (49)

$$18 \quad \chi = \frac{1}{l} \sum_{i=1}^l \left[\frac{1}{2} \times \frac{\bar{n}_o}{\sigma_{\bar{n}_o}} \times \log \frac{\bar{n}_p}{\bar{n}_o} \right]^2 \quad (3)$$

19 from which we estimate a likelihood, \mathcal{L} ,

$$20 \quad \mathcal{L} = \exp(-\chi) \quad (4)$$

21 where l is the number of TL signals (or thermometers) selected in TL temperature range
22 (27), (here $l=4$), $\sigma_{\bar{n}_o}$ is the measured error on \bar{n}_o . To account for the measurement
23 uncertainties in the kinetic parameters, we randomly pick the kinetic parameters within
24 its error range for each thermal history. We run the model for large number of thermal
25 histories (300,000 iterations) to ensure that we explore a wide range of possible
26 solutions.

27 Finally, the thermal histories that best fit the data are selected using a rejection
28 algorithm that satisfies the criterion $\mathcal{L} > R$, where R is a random number between 0 and 1.
29 A probability density distribution is then constructed by counting the number of accepted
30 thermal histories passing through grid cells, which are generated by dividing the time-
31 temperature space (0-100 kyr ago and -50 to 50 °C) into 100×100 cells. This approach is

1 commonly used in different thermochronometric studies (36,41,46, 51-52). The inversion
2 results for all the samples are shown in Figure S1.

3 We constrain the temperature at present and at the end of LGM, 17 kyr ago. As
4 mentioned above, the timing of end of LGM or complete removal of icecap is partly
5 uncertain. The top four samples were most like exposed since 17 kyr ago (Lehmann et al.,
6 2020). The bottom sample was exposed sometime between 17 to 12 kyr ago (Lehmann
7 et al., 2020). To assess the influence it may have on our interpretation, we calculated the
8 temperature at different times (20, 17, 15 and 12 kyr ago), which is shown in Figure S2(A-
9 B). It is important to note that temperature is nearly the same for the deglaciation period
10 of 20-15 kyr ago, which is expected as we use the Greenland $\delta^{18}\text{O}$ record. As result, the
11 estimated temperature at the end of the LGM remain relatively insensitive to the timing
12 of deglaciations. However, the temperature offset is significantly lower if the deglaciation
13 occurred only at 12 kyr ago, which would only apply to the lowest sample.

14 Mean temperature difference: To estimate the mean temperature difference between the
15 LGM and the present in the Mer de Glace area, we calculate the weighted mean and
16 standard deviation using the results from the inversion for the five analyzed samples and
17 assuming that all the errors are independent. The results are shown in Figure S2(E-H).

18 **2.2 Temperature model**

19 A linear regression model (29) that calculates the difference, i.e., surface offset, between
20 the rock surface and the air temperature for a given potential incoming solar radiation
21 (PSIR) was fitted with surface temperature measurements collected at the Aiguille du
22 Midi (3842 m, Mont Blanc massif) between 2008 and 2018.

23 The surface temperature was measured at a hourly time step at a depth of 10 cm
24 and then aggregated into mean annual values. Three measurement points were taken in
25 the south-exposed face of the Aiguille du Midi, two on the east face, two on the north face
26 and two on the west face in sub-vertical rock walls. In addition, temperature measured
27 at 30 cm in three 10-m-deep boreholes were also used (one on the north-west exposed
28 rock face, one on the north-east and one on the south-east) in slopes angles ranging from
29 55 to 80°. The last three sensors and one of the three sensors installed on the south face
30 are usually covered by snow during winter due to local topographical setting while all
31 other sensors remain in snow free conditions. Snow cover influences the registered
32 surface temperature due to both its thermal insulation effect and its high albedo. Thereby,

1 the surface temperature sample is representative of most alpine bedrock settings. The
2 measurements installations and settings as well as the rock surface temperature
3 characteristics are reported in (29). For this study, a total of 78 mean annual rock surface
4 temperature points were available to calibrate the regression model.

5 The air temperature has been measured continuously on top of the Aiguille du
6 Midi by Météo France since 2007. Daily air temperature values were also aggregated in
7 annual mean temperature. Finally, the PISR was calculated for a 1-m-resolution DEM of
8 the Aiguille du Midi, which was built up from a terrestrial laser-scanning point cloud
9 (acquired by L. Ravanel and processed by E. Ployon and F. Magnin) using the Spatial
10 Analyst toolbox from ArcGIS® (ESRI). As a potential value, the solar radiation was
11 calculated at a hourly time step over one full year assuming no atmosphere
12 (transmittance value of 1) and then converted into a mean annual value. PISR values were
13 then extracted at location of surface temperature from the 1 m resolution PISR map. The
14 following model was then calibrated: $SO = 0.0023 \times PISR + 0.75$. The results are shown in
15 Figure S3.

16 The model was used to calculate possible surface offset at bedrock sample
17 locations by mapping the PISR over a 2 m DEM generated from a point cloud acquired
18 and provided by the IGE (University Grenoble-Alpes, CNRS, IRD) within the GlacioClim
19 observation service (Fig. S4). Similarly to model calibration, the PISR was extracted at
20 bedrock sample location to calculate the offset with the linear regression.

21 Finally, we estimated the present temperature at each sample location by adding
22 the temperature offset to the estimated air temperature. The air temperature at each
23 sample location was estimated using the mean annual air temperature in Chamonix and
24 scaling it with altitude assuming a temperature lapse rate equal to 0.55 °C per 100 meter.

25 ***2.3 Inversion of paleo ice-extents into ELA fields***

26 We use a formal inversion approach (22) to invert the observed ice extent into spatially
27 variable Equilibrium Line Altitudes (ELAs). This approach consists of imposing a mass
28 balance rate to an ice flow model and find the range of ELA fields that can reproduce the
29 observed LGM ice-extent.

30 To simulate the ice flow, we solve the shallow ice approximation (51) and account
31 for the effect of flexural isostasy to adjust the elevation due to the flexure of the
32 lithosphere under the weight of the modelled ice-cap. The ensemble of equations being

1 solved are presented in (22,52). For the mass balance rate, M , we assume a standard
2 linear function (54-57):

$$3 \quad M = \min(\beta(S(x, y) - ELA(x, y)), c) \quad (5)$$

4 where S is the ice surface elevation, ELA is the elevation of the equilibrium line altitude,
5 β is the mass balance gradient and c is the maximum accumulation rate. To keep the
6 number of unconstrained parameters low, we assume that β is identical for the ablation
7 and accumulation areas, even though the mass balance gradient is often different in the
8 accumulation and ablation zones.

9 The inversion then consists of running the ice flow model iteratively until a
10 spatially varying ELA field that enables to fit the observed ice extent is found. To be able
11 to run a large number of models, the code is accelerated using Graphic Processing Units
12 (52). The model is run until steady state and we assume that the maximum ice extent was
13 synchronous for all the observed moraines, which is reasonable given the dating errors
14 of about 2 to 4 ka (25). We regularize the problem by assuming a smooth solution using
15 a Tikhonov regularization (58-59). Each inversion includes about 1000 forward ice flow
16 models.

17 Višnjević et al. (2020) (22) repeated the inversion 27 times for a set of possible β
18 and c . They also varied the sliding parameter, the elastic thickness and the
19 inversion parameters. We complemented these results with 12 additional inversions to
20 fully explore the range of possible solutions and in particular quantify the tradeoff that
21 exists between precipitation and temperature. All the inversion results reported here
22 were made assuming that the mass balance gradient, β , is lower or equal to the one
23 observed at present, i.e., 0.01 1/a (60). c was varied between 0.25 and 2 m/a. The
24 maximum winter accumulation rate observed at present is equal to 1.71 m/a (Huss et al.,
25 2008).

26 We use an existing LGM ice extents for the Alps (24) and the SRTM data for
27 topography. The ensemble of model parameters is reported in (22).

28 Finally, we convert the inferred the ELA field into temperatures and precipitation
29 rates at the Mer de Glace (Fig. 4). The difference of altitude between the LGM and present
30 ELA is converted into a temperature difference using the observed altitudinal
31 temperature lapse rate (0.55°C per 100 m) for each set of β and c . The difference of
32 precipitation is simply taken as the difference between c and the currently observed

1 winter accumulation rate. Although we do not account for local effects such as
2 surrounding topography, we find a general agreement in temperature changes
3 throughout the Alps.

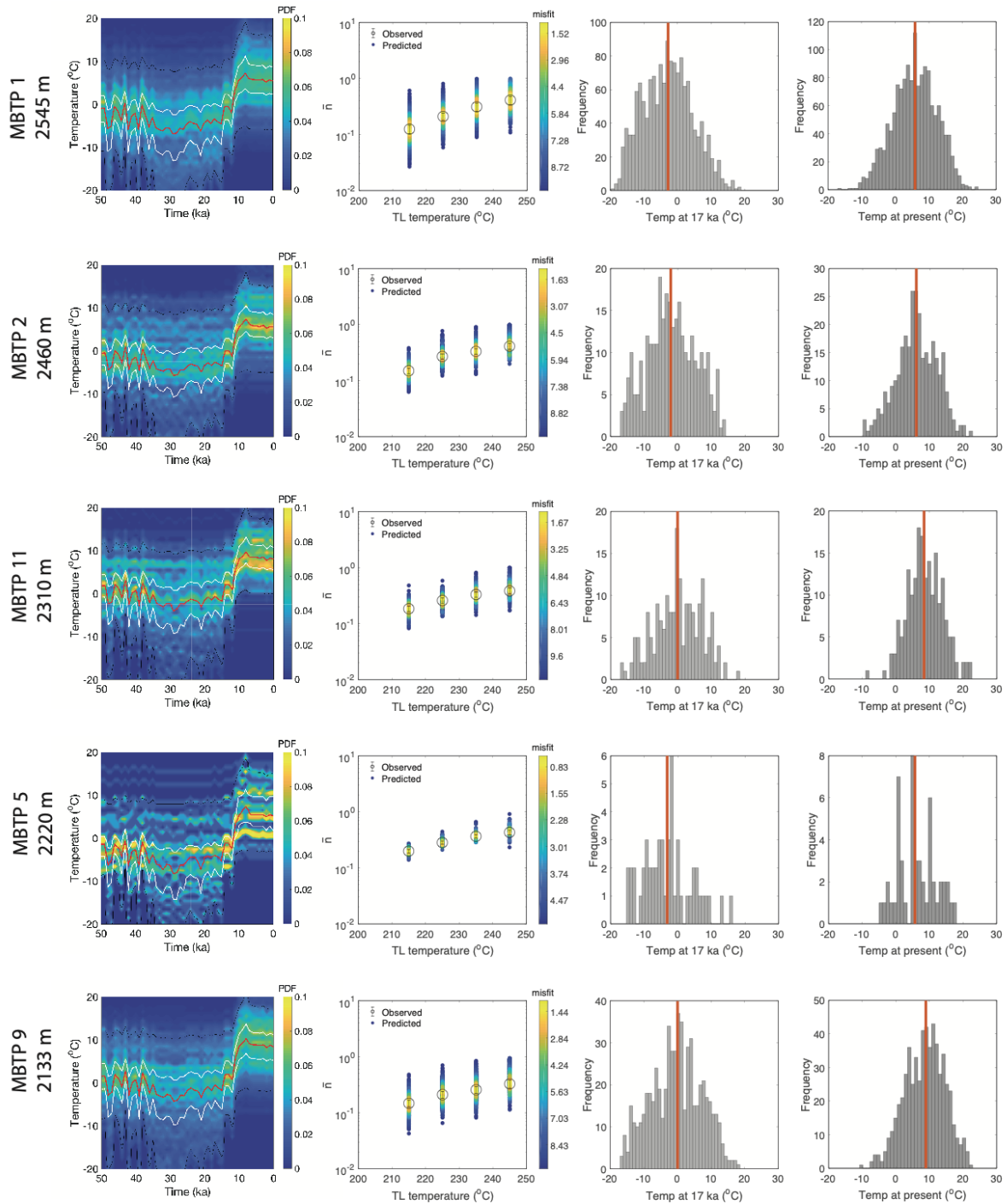
4 **2.4 Ice extents for different temperatures**

5 To illustrate the effect of temperature change on the ice extent we ran three forward
6 simulations assuming that the temperature was 8.5, 5 and 3.5 °C colder than present, β is
7 equal to 0.01 1/a and c is equal to 0.25 m/a, so 85% drier than at present. The results
8 show that the ice was not that different between 3.5 and 5 °C and considerably larger for
9 8.5 °C (Fig. S5).

10 **Supplementary Materials References**

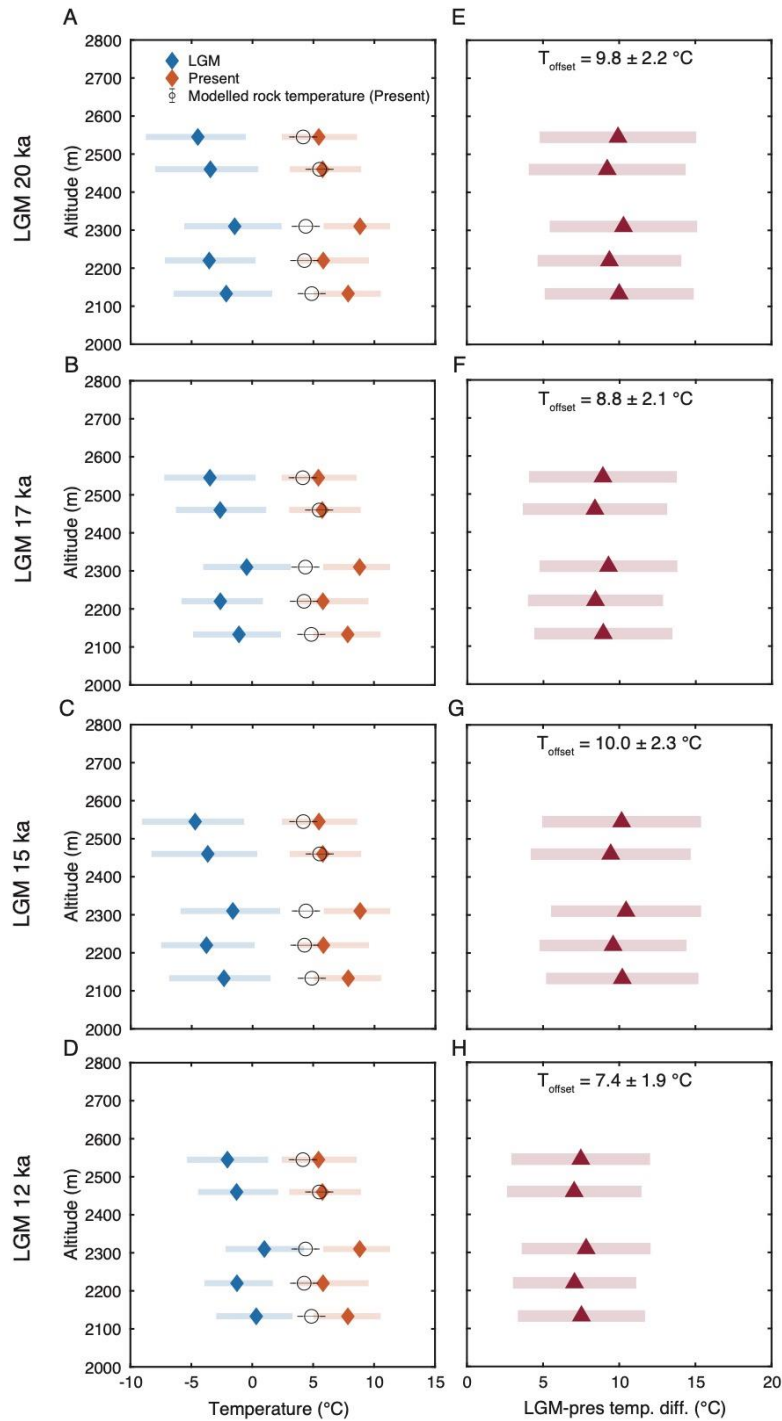
- 11 32. Aitken, M.J. *Thermoluminescence dating* (1985).
12 33. Ronca, L.B. & Zeller, E.J.. Thermoluminescence as a function of climate and
13 temperature. *American Journal of Science*, **263**(5), 416-428 (1965).
14 34. Durrani, S.A., Prachyabrued, W., Christo-Doulides, C., Fremlin, J.H., Edgington, J.A.,
15 Chen, R. & Blair, I.M. Thermoluminescence of Apollo 12 samples: implications for
16 lunar temperature and radiation histories. In *Lunar and Planetary Science*
17 *Conference Proceedings*, **3**, 2955-2969 (1972).
18 35. Durrani, S.A., Khazal, K.A.R. & Ali, A.. Temperature and duration of the shadow of
19 a recently-arrived lunar boulder. *Nature*, **266**(5601), 411-415 (1977).
20 36. Biswas, R.H., Herman, F., King, G.E. & Braun, J. Thermoluminescence of feldspar
21 as a multi-thermochronometer to constrain the temporal variation of rock
22 exhumation in the recent past. *Earth and Planetary Science Letters*, **495**, 56-68
23 (2018).
24 37. Tachiya, M. & Mozumder, A. Decay of trapped electrons by tunnelling to
25 scavenger molecules in low-temperature glasses. *Chemical Physics Letters*, **28**(1),
26 87-89 (1974).
27 38. Huntley, D.J.. An explanation of the power-law decay of luminescence. *Journal of*
28 *Physics: Condensed Matter*, **18**(4), 1359-1365 (2006).
29 39. Wintle, A.G. Anomalous fading of thermo-luminescence in mineral
30 samples. *Nature*, **245**(5421), 143-144 (1973).
31 40. Kars, R.H., Wallinga, J. & Cohen, K.M. A new approach towards anomalous fading
32 correction for feldspar IRSL dating—tests on samples in field
33 saturation. *Radiation Measurements*, **43**(2-6), 786-790 (2008).
34 41. King, G.E., Herman, F. & Guralnik, B. Northward migration of the eastern
35 Himalayan syntaxis revealed by OSL thermochronometry. *Science*, **353**(6301),
36 800-804 (2016a).
37 42. Duller, G.A.T. Behavioural studies of stimulated luminescence from
38 feldspars. *Radiation Measurements*, **27**(5-6), 663-694 (1997).
39 43. Grün, R. & Packman, S.C. Observations on the kinetics involved in the TL glow
40 curves in quartz, K-feldspar and Na-feldspar mineral separates of sediments and
41 their significance for dating studies. *Radiation measurements*, **23**(2-3), 317-322
42 (1994).

- 1 44. Pagonis, V., Morthekai, P. & Kitis, G. Kinetic analysis of thermoluminescence glow
2 curves in feldspar: evidence for a continuous distribution of
3 energies. *Geochronometria*, **41(2)**, 168-177 (2014).
- 4 45. Strickertsson, K.. The thermoluminescence of potassium feldspars—glow curve
5 characteristics and initial rise measurements. *Nuclear Tracks and Radiation*
6 *Measurements*, **10(4-6)**, 613-617 (1985).
- 7 46. King, G.E., Herman, F., Lambert, R., Valla, P.G. & Guralnik, B. Multi-OSL-
8 thermochronometry of feldspar. *Quaternary Geochronology*, **33**, 76-87 (2016b).
- 9 47. Bøtter-Jensen, L., Thomsen, K.J. & Jain, M. Review of optically stimulated
10 luminescence (OSL) instrumental developments for retrospective
11 dosimetry. *Radiation Measurements*, **45(3-6)**, 253-257 (2010).
- 12 48. Svensson, A., Andersen, K.K., Bigler, M., Clausen, H.B., Dahl-Jensen, D., Davies,
13 S.M., Johnsen, S.J., Muscheler, R., Parrenin, F., Rasmussen, S.O. & Roethlisberger,
14 R. A 60 000 year Greenland stratigraphic ice core chronology. *Climate of the Past*,
15 **4**, 44-57 (2008)
- 16 49. Wheelock, B., Constable, S. & Key, K.. The advantages of logarithmically scaled
17 data for electromagnetic inversion. *Geophysical Journal International*, **201(3)**,
18 1765-1780 (2015).
- 19 50. Herman, F., Rhodes, E.J., Braun, J. & Heiniger, L. Uniform erosion rates and relief
20 amplitude during glacial cycles in the Southern Alps of New Zealand, as revealed
21 from OSL-thermochronology. *Earth and Planetary Science Letters*, **297(1-2)**, 183-
22 189 (2010).
- 23 51. Gallagher, K.. Transdimensional inverse thermal history modeling for
24 quantitative thermochronology. *Journal of Geophysical Research: Solid*
25 *Earth*, **117(B2)** (2012).
- 26 52. Višnjević, V., Herman, F. & Podladchikov, Y. Reconstructing spatially variable
27 mass balances from past ice extents by inverse modeling. *Journal of*
28 *Glaciology*, **64(248)**, 957-968 (2018).
- 29 53. Hutter, K. *Theoretical glaciology: material science of ice and the mechanics of*
30 *glaciers and ice sheets*. Springer (1983).
- 31 54. Meier, M.F. Proposed definitions for glacier mass budget terms. *Journal of*
32 *Glaciology*, **4(33)**, 252-263 (1962).
- 33 55. Mayo, L.R. Glacier mass balance and runoff research in the USA. *Geografiska*
34 *Annaler: Series A, Physical Geography*, **66(3)**, 215-227 (1984).
- 35 56. Oerlemans, J., & N. C. Hoogendoorn. Mass-balance gradients and climatic
36 change. *Journal of Glaciology*, **35(121)**, 399-405 (1989).
- 37 57. Giesen, R.H. & Oerlemans, J. Calibration of a surface mass balance model for
38 global-scale applications. *The Cryosphere*, **6(6)**, 1463-1481 (2012).
- 39 58. Tikhonov, A.N. On the solution of ill-posed problems and the method of
40 regularization. In *Doklady Akademii Nauk*, Russian Academy of Sciences, **151(3)**,
41 501-504. (1963).
- 42 59. Aster, R.C., Borchers, B. & Thurber, C.H.. *Parameter estimation and inverse*
43 *problems*. Elsevier (2018)
- 44 60. Rabatel, A., Dedieu, J.P. & Vincent, C. Using remote-sensing data to determine
45 equilibrium-line altitude and mass-balance time series: validation on three
46 French glaciers, 1994–2002. *Journal of Glaciology*, **51(175)**, 539-546 (2005).
- 47 61. Huss, M., Bauder, A., Funk, M. and Hock, R. Determination of the seasonal mass
48 balance of four Alpine glaciers since 1865. *Journal of Geophysical Research: Earth*
49 *Surface*, **113(F1)** (2008).



1

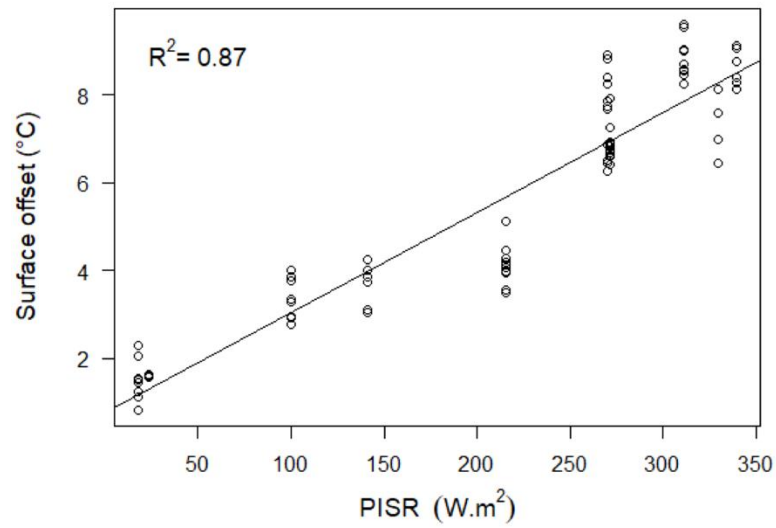
2 **Figure S1: Inversion of thermoluminescence data.** The first column corresponds to
 3 inferred probability density functions of the temperature histories. The second column
 4 shows the fit to the observed data, \bar{n}_ρ . The third and fourth columns depict the 1-d
 5 marginals of probability density functions of temperature at the end of the LGM and the
 6 present, respectively.



1

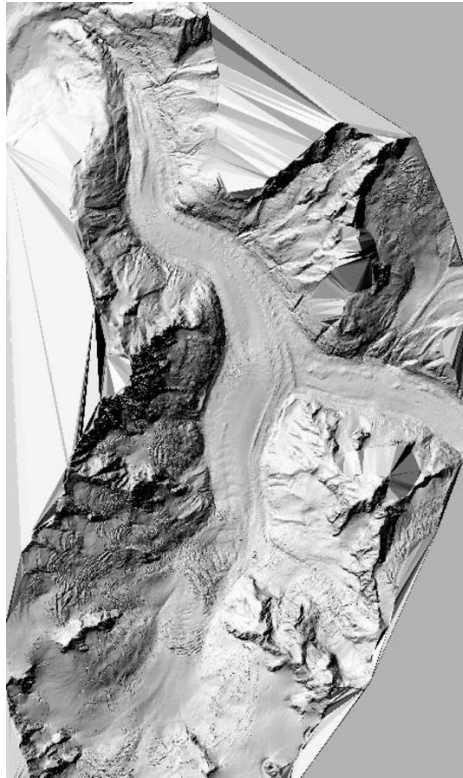
2 **Figure S2: Estimated temperature differences at different times (20, 17, 15 and 12**
 3 **kyr ago).** (A) to (D) are the estimated temperatures. (E) to (H) are the estimated
 4 temperature differences between the LGM and the present. The results show that the
 5 temperature differences between the LGM and today was similar at 20, 17 and 12 kyr
 6 ago.

1



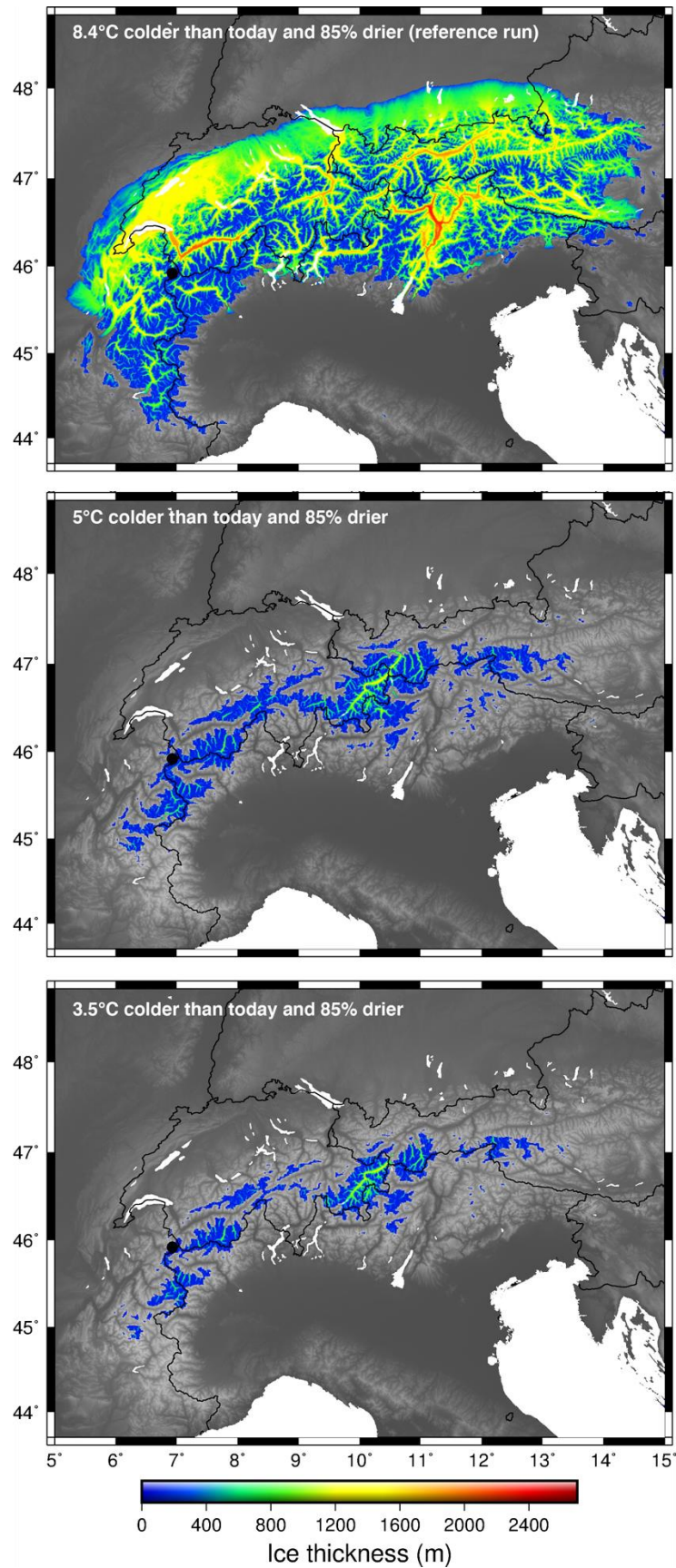
2

3 **Figure S3: Estimated temperature offset between air and rock temperature.** The
4 Linear regression model explaining the Surface Offset with the potential incoming solar
5 radiation (PISR) where the samples were collected (Fig. 1).



1

2 **Figure S4:** Hillshade of the 2-m resolution DEM generated for the Mer de Glace
3 and used to estimate the offset temperature (Fig. S3).



1
2
3
4

Figure S5: Ice thickness for 3 forward runs assuming that β is equal to 0.01 1/a and c is equal to 0.25 m/a.

1 **Table S1. Thermoluminescence results and parameters.** The \dot{D} values are from Lehmann et
2 al. (2020). We do not report the errors for the thermal decay parameters (E, s and b). The
3 estimated assuming an arbitrary error of 5%.

	TL (°C)	Growth			Thermal decay			Athermal decay	Natural TL (\bar{n}_{obs})		
		\dot{D} (Gy/ka) *	D_0 (Gy)	a	E (eV)	$\log_{10}(s)$	b	$\log_{10}(p^1)$	Uncorrected	NCF	Corrected
MBTP 1	210-220	7.39 ± 0.16	766 ± 51	1.00 ± 0.09	1.24	11.62	1.46	-6.02 ± 0.08	0.17 ± 0.03	1.36 ± 0.04	0.13 ± 0.02
	220-230		690 ± 46	1.00 ± 0.11	1.28	11.69	1.45	-6.29 ± 0.14	0.28 ± 0.04	1.34 ± 0.03	0.21 ± 0.03
	230-240		638 ± 43	1.00 ± 0.13	1.31	11.75	1.45	-7.10 ± 0.94	0.41 ± 0.07	1.31 ± 0.03	0.31 ± 0.05
	240-250		559 ± 40	1.00 ± 0.26	1.35	11.79	1.45	<-20 ± 0.00	0.53 ± 0.09	1.29 ± 0.03	0.41 ± 0.07
MBTP 2	210-220	7.35 ± 0.15	796 ± 32	1.00 ± 0.03	1.25	11.73	1.47	-6.36 ± 0.20	0.23 ± 0.03	1.51 ± 0.02	0.15 ± 0.02
	220-230		500 ± -	1.00 ± 0.00	1.29	11.82	1.46	-6.64 ± 0.39	0.40 ± 0.04	1.48 ± 0.02	0.27 ± 0.03
	230-240		644 ± 27	1.05 ± 0.19	1.32	11.89	1.46	-7.62 ± 3.74	0.48 ± 0.06	1.46 ± 0.03	0.33 ± 0.04
	240-250		559 ± 29	1.18 ± 0.24	1.36	11.96	1.46	<-20 ± 0.00	0.59 ± 0.07	1.43 ± 0.03	0.41 ± 0.05
MBTP 5	210-220	7.73 ± 0.16	770 ± 30	1.00 ± 0.04	1.23	11.47	1.51	<-20 ± 0.00	0.36 ± 0.02	1.82 ± 0.03	0.20 ± 0.01
	220-230		710 ± 24	1.00 ± 0.00	1.27	11.54	1.51	<-20 ± 0.00	0.51 ± 0.03	1.80 ± 0.03	0.28 ± 0.02
	230-240		631 ± 20	1.02 ± 0.13	1.30	11.59	1.51	<-20 ± 0.00	0.65 ± 0.05	1.78 ± 0.03	0.37 ± 0.03
	240-250		559 ± 18	1.07 ± 0.13	1.34	11.63	1.51	<-20 ± 0.00	0.76 ± 0.07	1.76 ± 0.03	0.43 ± 0.04
MBTP 9	210-220	7.07 ± 0.15	773 ± 41	1.00 ± 0.03	1.25	11.63	1.49	-6.13 ± 0.09	0.26 ± 0.03	1.73 ± 0.08	0.15 ± 0.02
	220-230		680 ± 37	1.00 ± 0.01	1.29	11.72	1.49	-6.18 ± 0.10	0.36 ± 0.05	1.72 ± 0.08	0.21 ± 0.03
	230-240		625 ± 40	1.18 ± 0.33	1.32	11.79	1.49	-6.33 ± 0.17	0.44 ± 0.06	1.71 ± 0.09	0.26 ± 0.04
	240-250		502 ± 36	1.10 ± 0.27	1.36	11.85	1.49	-6.51 ± 0.24	0.56 ± 0.08	1.70 ± 0.09	0.33 ± 0.05
MBTP11	210-220	8.14 ± 0.17	707 ± 20	1.00 ± 0.01	1.24	11.52	1.49	<-20 ± 0.00	0.33 ± 0.03	1.81 ± 0.14	0.18 ± 0.02
	220-230		660 ± 18	1.00 ± 0.11	1.28	11.59	1.49	<-20 ± 0.00	0.46 ± 0.03	1.79 ± 0.14	0.26 ± 0.03
	230-240		593 ± 19	1.00 ± 0.13	1.32	11.65	1.49	<-20 ± 0.00	0.59 ± 0.04	1.77 ± 0.15	0.33 ± 0.04
	240-250		527 ± 18	1.00 ± 0.07	1.35	11.69	1.49	<-20 ± 0.00	0.67 ± 0.06	1.75 ± 0.15	0.38 ± 0.05

4